RESEARCH ARTICLE

ADVANCED FUNCTIONAL MATERIALS
www.afm-journal.de

Intercalated Graphene and Colloidal Quantum Dots for Multispectral Photodetection

*Seungbae Ahn, Ju Ying Shang, Suraj K. Patel, Erick Alvarado, Abdoulaye Ndao, and Oscar Vazquez-Mena**

Hybrid photodetectors with 2D materials and quantum dots (QDs) offer new opportunities for spectral detection given their high mobilities and spectral tunability, respectively. Herein, the study presents a novel architecture of alternating PbS QDs with graphene monolayers positioned at different depths and with independent contacts. This geometry enables the probing of the photocurrent depth profile and therefore of different spectral bands. The study realizes devices with up to five graphene layers and five QD layers intercalated, using only one type of QDs (Single-Bandgap devices) with an exciton absorption peak at 920 nm, as well as devices with different types of QDs (Multi-Bandgap devices) with exciton peaks at 850, 1190, and 1350 nm. Since the absorption depth and photoresponse is wavelength dependent, each graphene has a different spectral response, which opens the path for spectral analysis. As expected, it is observed that top graphene layers have stronger response than deeper graphene layers, especially for short wavelengths. However, for the case of Multi-Bandgap devices, a negative photoresponse coefficient is even observed for longer wavelengths, showing stronger response for deeper layers than for top layers. This intercalated architecture can be used for compact multispectral photodetection without any diffractive or beam splitting component.

1. Introduction

The development of compact and broadband photodetectors with spectral analysis capabilities is essential for material composition and object identification analysis[1–6] in applications such as remote and point-of-care health care,[7–9] water and environmental quality monitoring,[10] gas detection,[11] counterfeit detection,[12] food quality inspection,[13,14] and autonomous transportation[15] among others. Building a large network of such sensors able to supply information continuously is also critical to collect large data sets for machine learning algorithms for those same applications.[16] Furthermore, incorporating multispectral sensor networks into mobile personal devices and autonomous vehicles can lead to novel capabilities in personal health-care and safer transport. The implementation of such networks of sensors requires low-cost, compact, and light weight multispectral light detection technologies. For visible (Vis) and near-infrared (NIR) wavelengths, Bayer filters, stacked p-n junctions, and lenslets arrays have been integrated into complementary metal-oxide semiconductor (CMOS) detectors to enable compact architectures.[5,17–20] However, these devices are usually limited to Si absorption and cannot operate beyond the NIR. Going beyond $\lambda \approx 1000$ nm, most conventional multispectral technologies require dispersive optics such as beam splitters, arrays, or interferometers with large footprints. [21–25] Perovskites have also been used in stacked configurations but limited to Vis–NIR range.[26] For mid-wave infrared (MWIR) range, the use of epitaxial films like HgCdTe significantly increases the costs compared to Si or Ge detectors used in the Vis-NIR range. An alternative emerging route is nanomaterials such as 2D materials[27,28] and quantum dots.[29–31] with novel optoelectronic properties and capabilities in addition to their low temperature processing. For instance, two-band infrared photodetectors have been implemented using HgTe stacked colloidal quantum dot photodiodes.[29] Black phosphorous has also been used as mid-infrared spectrometer using bias-dependent spectral tuning and machine learning.[27] QDs patterned in a lateral architecture have allowed for a three channel multispectrometer reaching the MWIR range with HgTe QDs on a readout integrated circuit platform.[32,33] Herein, we present a novel architecture for compact and broadband multispectral photodetection based on a PbS quantum dot (QD) films as light absorbing layer intercalated with graphene (Gr) charge collectors with independent electrodes to detect different spectral bands.

As it has been demonstrated previously, the hybrid system of graphene and PbS quantum dots works efficiently as a photoconductive detector both in single junction and intercalated

---

S. Ahn, J. Y. Shang, S. K. Patel, O. Vazquez-Mena
Aiiso Yufeng Li Family Department of Chemical and Nano Engineering
Center for Memory and Recording Research
Program in Materials Science and Engineering
University of California San Diego
9500 Gilman Drive, La Jolla, CA 92093, USA
E-mail: ovmena@ucsd.edu

E. Alvarado, A. Ndao
Department of Electrical and Computer Engineering
University of California San Diego
9500 Gilman Drive, La Jolla, CA 92093, USA

The ORCID identification number(s) for the author(s) of this article can be found under https://doi.org/10.1002/adfm.202409523

DOI: 10.1002/adfm.202409523

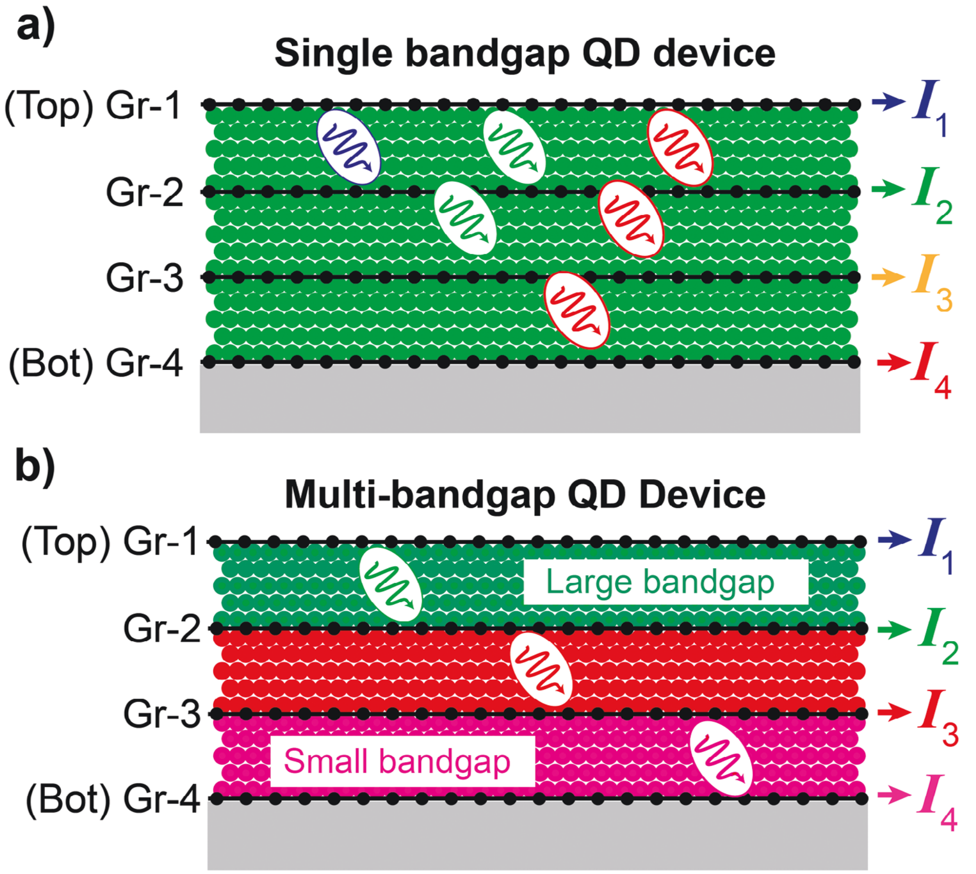

Figure 1. Device operation principle. Intercalated devices based on sequential stacking of QDs and graphene with independent electrodes to measure the current through each individual graphene monolayer (I_1 through I_4). QDs act as light absorbers and photocarrier generators. Graphene monolayers serve as independent charge collectors to collect photocarriers generated in adjacent, top and bottom, QD layers. a) Single-Bandgap devices have only one type of PbS QDs. Shorter wavelengths can be detected in the top layers due to the short penetration depth, while longer wavelengths are detected through the entire stack due to the longer penetration depths. b) Multi-Bandgap devices have PbS QDs of different sizes with decreasing bandgap from top to bottom. Short wavelengths are absorbed mainly at the top layers, while long wavelengths are absorbed mainly at bottom layers.

geometries.[34–40] The quantum dot layers absorb photocarriers and generate electron-hole pairs that are transferred to graphene. Graphene monolayers serve as independent charge collectors to collect photocarriers generated in adjacent, top and bottom, QD layers. In this work, we further develop this technology using intercalated devices with independent electrical contacts to each graphene layer at different depths, allowing to probe light penetration through the QD film and giving different spectral responses for each Gr layer. Our approach avoids any beam splitting, interferometers, filtering, or diffractive components with simultaneous recording of different graphene layers with their respective spectral bands. The principle of operation is shown in **Figure** 1a for “Single-Bandgap” devices that contain only one size of PbS QDs. Due to the difference in absorption depth for different wavelengths, each graphene has a different spectral response. Short wavelengths with short penetration depths are absorbed mainly at the top layers while long wavelengths with deeper penetration depths are detected through the entire stack at top and bottom layers. We also realized “Multi-Bandgap” devices that integrate different sizes of QDs with decreasing bandgaps from top to bottom as shown in Figure 1b. This enables to expand the spectral range of operation and tune the light absorption profile with short wavelengths absorbed at the top layers and longer wavelengths absorbed at the bottom layers. Furthermore, in the Multi-Bandgap devices, we obtain a negative photoresponse coefficient behavior for long wavelengths, i.e., stronger photoresponse at deeper levels. This can facilitate wavelength identification and spectral analysis in the infrared region without any dispersive or interferometer components.

2. Device Fabrication

The fabrication of the devices is challenging as it requires not only the sequential deposition of graphene layers and quantum dots to produce intercalated devices, but also implementing individual contacts for each graphene layer. To fabricate the devices, we used graphene monolayers grown by chemical vapor deposition on copper obtained from a commercial supplier (Graphenea, Spain). The graphene transfers were based on wet transfer by dissolving the copper with ammonium persulfate and using PMMA as supportive layer on top of graphene, followed by the removal of the PMMA in acetone and isopropanol.[41] The colloidal PbS QDs were synthesized using lead oxide (PbO) and bis(trimethylsilyl) sulfide as PbS precursors to obtain a solution of oleic acid

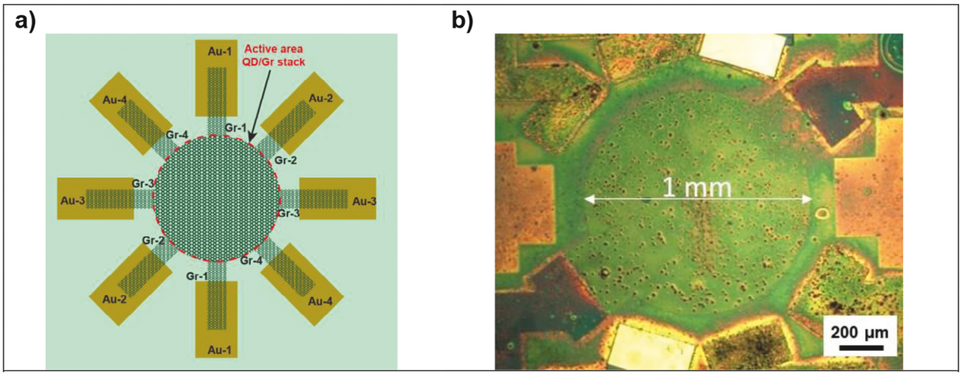

Figure 2. Device scheme and image. a) Device diagram that shows an array of gold electrodes contacting different graphene layers at different depths in an intercalated Gr/PbS QD stacked film. b) A fabricated device shows the gold electrodes and a central stacked active device with intercalated Gr/PbS QD devices. The central active circular area has a diameter of 1 mm.

functionalized QDs dissolved in toluene as described elsewhere.[42] The PbS QD layers were prepared by spin coating of the QDs in toluene solution, followed by a ligand exchange to replace the long oleic acid chains by tetrabutylammonium iodide (TBAI) to facilitate charge transport from QD to QD. The schematic geometry of the devices from the top view is shown in **Figure** 2a, showing a circular array of electrodes. A pair of opposite electrodes serve as source and drain contacts to apply a voltage and collect the current from each graphene layer. The graphene layers are patterned in a circular geometry with two side arms connected to their corresponding contacts. A fabricated device observed under the optical microscope is shown in Figure 2b, illustrating the contacts in a circular arrangement with a central circular shaped area with the graphene stacked layers. The active area of this device is the central circular section with a 1 mm diameter, composed of graphene layers, each with its own electrical contacts at different depths intercalated with PbS QD layers.

An overview of the fabrication process flow is described in **Figure** 3 from a sideview perspective. A more detailed and extended process flow is shown in the Supporting Information (Figure S1, Supporting Information). Figure 3 shows a process for 3 graphene and 3 QD layers, but this sequence is valid for any number of layers. The devices were built on a Si wafer 500 µm thick with a 300 nm thick silicon oxide on top. The wafers had an array of prepatterned electrodes made by lithography and lift-off as shown in Figure 3a with the pattern shown in Figure 2a,b. The contacts consist of a 10 nm layer of chrome as adhesive layer, followed by 100 nm of gold as conductive layer, and then 100 nm of copper on top (Cr/Au/Cu) that serves as a protective layer during PbS QD etching. The fabrication of the intercalated devices starts with the PMMA-supported wet transfer of the first graphene layer which corresponds to the "bottom" graphene layer. After transfer, this graphene layer is patterned by lithography and O_2 plasma etching (Figure 3b), defining a circular structure in the middle of the contact array, with two short channels to connect to a first set of electrodes. After the first layer of graphene is patterned, the first layer of QDs is deposited. This is done by spin coating of QDs followed by TBAI ligand exchange.[43–45] Then, before transferring a second graphene layer, the first layer of QDs is patterned by lithography and $H_2/CH_4/Ar$ plasma dry etching to expose the second set of Au contacts (Figure 3c). During this etching process, the 100 nm thick copper protective layer helps to protect the gold contacts from the etching plasma. After the etching process, and before removing the patterned resist, an ammonium persulfate solution is used to remove the copper protective layer, leaving a second set of Au/Cr contacts exposed. Then, a second "middle" graphene layer was transferred by wet transfer (Figure 3d) following the same procedure as the first "bottom" layer. This layer sits on top of the first layer of QDs, but it gets in electrical contact with the second set of Au/Cr electrical contacts. This layer is again patterned forming a circular pattern and two channels to the second set of contacts. Then, a second layer of QDs is deposited by spin coating followed by ligand exchange. This second layer was also patterned by lithography and $H_2/CH_4/Ar$ plasma etching, removing the QDs from a third set of contacts (Figure 3e). The copper protective layer is then also removed by ammonium persulfate. Finally, a third graphene layer is transferred and patterned (Figure 3f), followed by the spin coating of a third layer of QDs which may not require further patterning (Figure 3g). This procedure can be repeated several times to add more QD and graphene layers as desired. The total number of prepatterned electrodes can also be adapted as required. This general procedure can be used to get devices with single or multiple bandgap quantum dots. In order to control the thickness of each QD layer, it is important to calibrate the thickness for each spin coating step. The typical thickness for a single coating step is in the ≈10–30 nm range depending on the QD size and solution concentration. For example, for QDs with a bandgap of 1.26 eV ($\lambda \approx 1000$ nm), each spin coating step results in a 15 nm thick layer of QDs. Therefore, to obtain a film of 300 nm, we spin coat a total of 20 times (layers). The circular active area has a diameter of 1 mm. After fabrication, the device was characterized with a 2400 Keithley sourcemeter and a Xe lamp with a monochromator.

3. Optoelectronic Characterization

Figure 4a shows a schematic description of the Single-Bandgap QD device using only one type of QDs. The device consists of four layers of PbS QDs intercalated with four graphene charge collectors. The top QD layer is only 150 nm thick and the three sub-

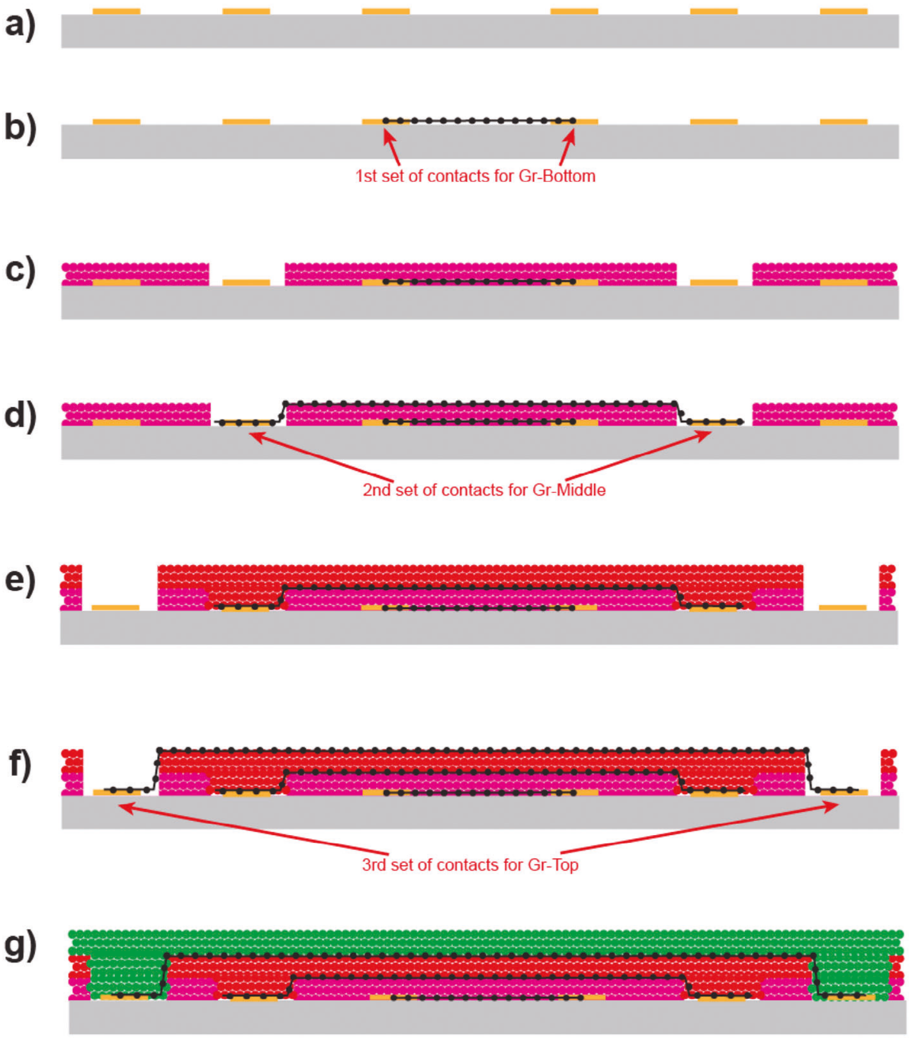

Figure 3. Fabrication process. a) Prepatterned electrodes with Cr as adhesive layer, Au as electrical contact and Cu as protective layer. b) Graphene wet transfer and patterning by lithography and O_2 plasma dry etching. c) Spin coating and ligand exchange of PbS QDs, followed by dry etching pattering using $H_2/CH_4/Ar$ plasma. The goal of the patterning is to expose the contacts for the next graphene monolayer. Cu protective layer is removed in ammonium persulfate to leave Cr/Au contacts. d) Wet transfer of the next graphene layer on top of the first QD layer, followed by plasma dry etching pattern. This graphene is contacted by the second set of electrodes. e) Coating of PbS QDs and patterning similar to step "b", exposing the contacts for next graphene layer. f) Wet transfer of 3rd graphene layer followed by plasma etching patterning. g) Coating of 3rd QD layer by spin coating and ligand exchange. The sequence of "d" and "e" can be repeated to build the intercalated stack varying the type of QDs. Each QD layer requires multiple spin coating steps since a single spin coating layer results in thickness of ≈15–30 nm depending on the QD size. A more detailed process flow is shown in the Supporting Information.

sequent layers are 300 nm thick and therefore located at depths of z = 150, 450, 750, and 1050 nm respectively. Each graphene layer, labeled as Gr-1 to Gr-4 from top to bottom, has its own set of contacts as shown in Figure 4a. The thickness of 150 nm for top and 300 nm for the rest of the QD layers was chosen to ensure that photocarriers always have a graphene layer at a distance of 150 nm, which is below the typical diffusion length of PbS QDs reported in literature,[43,46–49] ensuring that photocarriers can reach the graphene layers for effective charge collection. The resistance for each graphene was measured with a 2401 Keithley applying a voltage of 40 mV giving R = 11.1, 7.2, 6.1, and 11.4 kΩ for Gr-1 to Gr-4, respectively. The I/V curve for Gr-4 is shown in the Figure S2a (Supporting Information). The I/V current between Gr-4 and Gr-3 through the bottom QD layer is shown in Figure S2b (Supporting Information) showing a much higher resistance of 1.21 MΩ. The optoelectronic measurements are carried with light incident from top with a monochromator. As the light penetrates, it is absorbed following the Beer-Lambert equation exp(-$\alpha(\lambda)$/z), where α is the absorption coefficient that typically decreases as the wavelength λ increases. As reported in previous works, the effect of graphene on the light absorption is negligible compared to the PbS QD light absorption.[35] The UV/Vis absorption spectrum of the PbS QDs is shown in the Figure S3a (Supporting Information), showing an exciton reso-

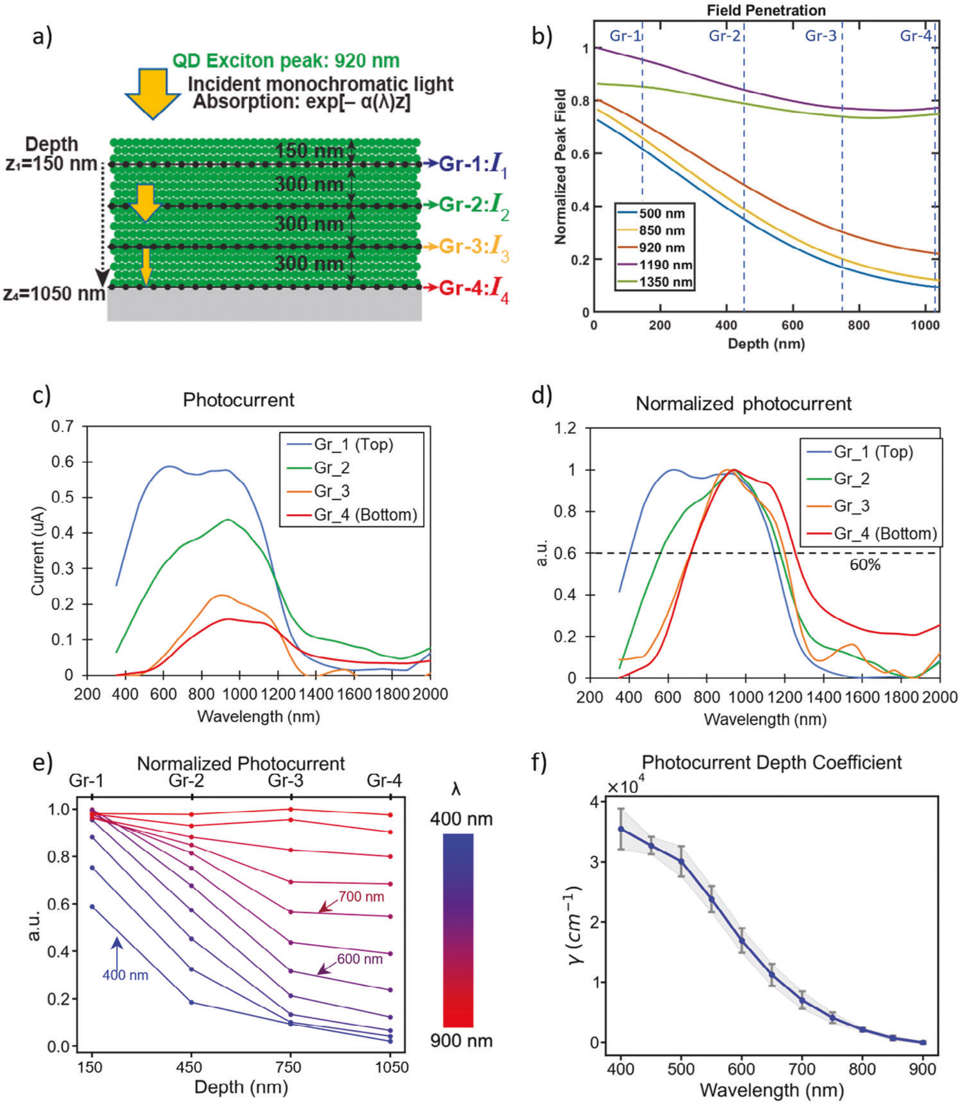

Figure 4. Single-Bandgap Device. a) Device scheme showing 4 graphene layers intercalated with 4 QD layers with top illumination assuming an exponential decay in light absorption. Each layer has the same type of QDs. b) FEM simulations of light penetration as a function of wavelength with dashed vertical lines indicating the positions of the graphene collectors. c) Photocurrent from each graphene layer at a bias voltage of 100 mV showing a different response for each graphene layer, with stronger response at top layer and decreasing for deeper layers. d) Photocurrent normalized to the maximum of each curve in "c", illustrating the different spectral response. e) Normalized photocurrent from "d" plotted at different depths corresponding to the location of the four graphene layers, showing shorter decays in photocurrent for shorter wavelengths. The traces correspond to $\lambda \approx 400-900$ nm in steps of 50 nm. f) Normalized photocurrent depth coefficient (γ) by assuming an exponential decay $\approx \exp(-\gamma z)$ similar to Beer–Lambert law.

nance peak near $\lambda \approx 920$ nm. Transmission electron microscopy (TEM) images of the QDs are shown in Figure S3c (Supporting Information). Finite element method simulations (CST Studio, Simulia, Dassault Systems) simulations of the light penetration (normalized field intensity vs depth) are shown in Figure 4b for $\lambda = 500$, 850, 920, 1190, and 1350, with the vertical dashed lines corresponding to the positions of the graphene collecting layers (Gr-1 to Gr-4). The simulations show the expected behavior of deeper penetration for longer wavelengths. In particular, $\lambda \approx 500$, 850, and 920 show a much shorter penetration probably due to the strong absorption as they are below or equal to the absorption threshold of the PbS QDs at $\lambda \approx 1000$ nm, whereas $\lambda \approx 1190$ and 1350 nm light wavelengths show much weaker absorption. The experimental measured photocurrent for each graphene layer under a bias voltage of 100 mV as a function of wavelength is shown in Figure 4c. The top graphene (Gr-1) has clearly the largest photocurrent since it experiences the largest photon flux, which leads to higher photocarrier generation and higher photocurrent. The photocurrent then decreases for deeper graphene layers as the light intensity decreases for deeper regions. However, it can also be observed that the top graphene layer (Gr-1) covers a broader spectral photoresponse compared to the bottom layer (Gr-4). Gr-1 also has its maximum photocurrent at a shorter wavelength of $\lambda \sim 600$ nm, while Gr-4 has its maximum photocurrent at $\lambda \approx 900$ nm. A slight increase in photoresponse for all monolayers is observed near $\lambda \approx 2000$ nm which may be due to midgap states and surface defects induced at Gr/QD interface. In order to compare the spectral responses, we used min-max normalization for each graphene layer, as plotted in Figure 4d. Gr-1 has a normalized response above >0.6 (dashed reference line in Figure 4d) in a broad range of $\Delta\lambda_{\text{Gr-1}} \approx 400-1150$ nm, while Gr-4 has a response above 0.6 in a narrower and red-shifted range of $\Delta\lambda_{\text{Gr-4}} \approx 700-1300$ nm. In the short wavelength range of $\lambda \approx 400-900$ nm, the normalized photocurrent of the top graphene Gr-1 is clearly higher than the rest of the layers, followed by Gr-2 and then by very similar responses from Gr-3 and Gr-4. This behavior is due to absorption depths increase with increasing wavelength for semiconductors.[50] As the top QD layers absorb the short wavelength photons, the bottom QD layers encounter much reduced number of photons, which results in less photogenerated carriers and less photocurrent collected by the bottom graphene layers. When longer wavelength photons are incident on the Single Bandgap device, they are not all absorbed by the top QD layers, due to the photons' lower energy which leads to less scattering and absorption. The longer wavelength photons penetrate deeper and are encountered at a higher number by the bottom layers, which results in higher photocurrents. Figure S4a (Supporting Information) shows absorption of the entire stacks indicating significant absorption up to $\lambda \approx 1300$ nm, in agreement with the normalized photocurrent showing significant response for all layers up to $\lambda \approx 1300$ nm as well in Figure 4d.

To study the decay in photoresponse through the graphene layers, we plot the normalized photoresponse as function of depth for different wavelengths as shown in Figure 4e. The discreet values in depth of z = 150, 450, 750, and 1050 nm correspond to the positions of the graphene layers in Figure 4a. This plot shows how short wavelengths from 400 to 600 nm show rapid decays close to an exponential decay that resembles the behavior for light absorption from the Beer-Lambert law. However, in the case of Figure 4e, we plot the normalized photocurrent, allowing for comparing between the spectral photoresponses of each graphene layer. For wavelengths longer than 700 nm, the decay is much slower and eventually the curves show a flat behavior indicating the same normalized photocurrent for all layers. The slower decay is indicative of the increase in absorption depth for increasing wavelength. At 900 nm, all four graphene layers are showing maximum normalized photocurrent, which matches with the exciton resonance peak of the QDs at 920 nm. Close to the exciton resonance wavelength, the absorption is higher due to exciton generation, leading to more photocarriers that results in higher photocurrent. Beyond $\lambda \sim 1200$ nm the response of all the layers decays as light in this range cannot excite photocarriers in the PbS QDs.

The curves in Figure 4e were fitted to an exponential, ~exp $(-\gamma z)$ (see Figure S5a, Supporting Information) to calculate the decay coefficient for the normalized photoresponse, which we call the "Photocurrent Depth Coefficient (γ)". It allows us to characterize the wavelength response of the Single Bandgap device, by combining the photocurrents of all graphene layers into one number for each wavelength. These coefficients are plotted in Figure 4f. Shorter wavelengths have higher coefficients, while longer wavelengths have lower, close to zero, coefficients, following a similar trend as the light absorption coefficient ($\alpha(\lambda)$). It should be noted that these two coefficients are not the same. While the absorption coefficient ($\alpha(\lambda)$) is a measure of light absorption penetration depth that depends essentially on the QDs, the photocurrent depth coefficient is a measure of photocurrent response as function of depth, therefore it involves not only the QDs, but also the electrical conduction mechanisms, especially the charge transfer between Gr and QDs. This penetration depth coefficient is not a figure of merit to evaluate the performance, but it allows to characterize the photoresponse as a function of depth for different wavelengths which is critical to identify the spectral components from an incoming light source. From the photocurrent depth coefficient, it is possible to estimate the wavelength of an incident light source.

The time response of the devices under $\lambda \approx 635$ nm is shown in **Figure 5a** (see time fittings in Figure S6a, Supporting Information). The rising response times from top to bottom (Gr-1 to Gr-4) are 120, 49, 81, and 59 ms, for an average of 77 ms. The recovery times have two components with fast components showing recovery times of 290, 160, 330, and 300 ms, for an average of 270 ms that account for ≈50% of the decay, and slower recovery times with a second slower component in the order of ≈2 s. The slower recovery times are usually associated with traps in the QDs that extend the lifetime of minority electrons carriers responsible for the photogain effect, resulting in slower recovery times.[51] This has been observed in similar hybrid Gr-PbS QD photodetectors.[38,40,52] Konstantatos et al. reported response times of 10 ms but recovery times with slow component of 2 s,[38] while Sun et al. reported both response and recovery times longer than 2 s[40] also associated with surface traps. The most promising route to increase the speed of the devices is to use top-bottom configurations whose response now requires current through the QD film that are faster because their response is determined by the much shorter lifetime of majority carriers. Top-Bottom contacts can reach much faster responses in the ≈1 µs – 20 ns range.[51,53] Using top-bottom configurations, Tang et al have demonstrated also fast responses of 24–59 ms using top-bottom configurations,[54] and Nikitskiy show fast responses of 10 ms using a top-ITO active layer on the Gr/QD interface.[55]

In order to expand the spectral range and enhance the spectral separation for different graphene layers, we implemented devices using 3 different types of PbS QDs of different sizes (Multi-Bandgap devices), with small size and large bandgap QDs to absorb short wavelengths, and larger size QDs with smaller bandgaps at the bottom to absorb longer wavelengths as shown in **Figure 6a**. The UV/Vis absorption spectra of the PbS QDs are shown in Figure S3b (Supporting Information), showing excitonic peaks at $\lambda \approx 850$ nm for QD-1, $\lambda \approx 1190$ nm for QD-2, and $\lambda \approx 1350$ nm for QD-3. Figure S3d (Supporting Information) show TEM images of the QDs. The devices have five layers of PbS QDs intercalated with five graphene layers with the following sequence from top to bottom: QD-1/Gr/QD-1/Gr/QD-2/Gr/QD-2/Gr/QD-3/Gr. The first QD layer has a thickness of ≈150 nm and the subsequent layers of 300 nm. Therefore, the graphene layers are located at depths of z ~ 150, 450, 750, 1050, and 1350 nm. Similar to the case of the single-bandgap devices, thicknesses were chosen to ensure effective charge transport and collection from the PbS QDs to Gr. The resistance for each graphene was measured with a 2401 Keithley applying a voltage of 40 mV giving R = 5.1, 2.5, 1.8, 3.0, and 4.08 kΩ for Gr-1 to Gr-5, respectively. The field penetration as a function of wavelength through the stack is shown in Figure 6b, showing the

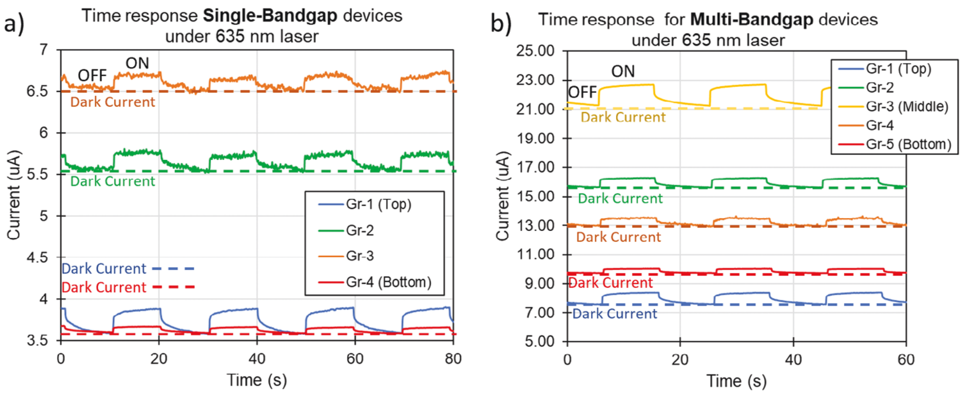

Figure 5. Time response. a) Single-bandgap device time response under $\lambda \approx 635$ nm illumination shows the rise of current under light and then recovering to the dark level. Gr-3 has the largest base current, but the top Gr-1 layer has the largest photocurrent. The average rise time for the four graphene layers is 77 ms and the average recovery time is 270 ms. b) Multi-bandgap device time response showing Gr-3 has the largest base current, as well as the largest photocurrent. The average rise time for the five graphene layers is 72 ms and the average recovery time is 210 ms.

expected deeper penetration depths for longer wavelengths. The photocurrent for each graphene layer in Multi-Bandgap device is shown in Figure 6c. This device achieves a broader spectral response, covering a range of λ:400–1500 nm, which is broader than λ:400–1200 nm for the Single-Bandgap device. However, the photoresponse from each graphene layer follows a different trend. The highest photocurrent is obtained by the Gr-3 (middle) layer. Then, Gr-1 (Top) and Gr-2 show similar photocurrent levels but lower than Gr-3, and then the lowest responses are obtained from Gr-4 and then from Gr-5 (Bottom). This is different from Single-Bandgap devices in Figure 4c in which the photocurrent decreases from top to bottom graphene layers. The simulations for light penetration from Figure 6b do not show any significant concentration of the field or light absorption at the Gr-3 position (depth = 750 nm), therefore, we think this enhancement is due to a more efficient charge collection mechanism between QD-2 type and Gr-3. This may be due to better charge transfer among the QDs related to perhaps better conductivity and mobility for QD-2, or improved charge transfer mechanisms from QD-2 film to Gr due to band alignment, built-in potential and surface state considerations. This indicates that to a detailed study on the efficiency of charge transfer from QDs to Gr as a function of QD size is required. Previously, it has been reported that even with QDs of the same composition such as PbS, the coupling and charge transfer from QDs to Gr changes with QD size.[42,49] The results in Figure 6c indicate there should be a strong photocarrier generation and coupling between QD_2 and Gr-3 that results in the strongest photocurrent at Gr-3 despite being at deeper levels than Gr-1 and Gr-2.

The main goal implementing the Multi-Bandgap devices is to extend the spectral response range and enhance the spectral splitting. To focus on the spectral response, we again used min-max normalization as shown in Figure 6d. This illustrates the difference in spectral response for each Gr layer, clearly showing a shift toward longer wavelengths for deeper graphene layers. This contrasts with the Single-Bandgap devices, in which all Gr layers had the same long wavelength limit response due to all QDs having the same bandgap. In the Multi-Bandgap case, Gr-1 (Top) has normalized response above 0.6 in the $\Delta\lambda_{Gr\_1} \approx 300$–950 nm range, while the Gr-5 (Bottom) shifts to $\Delta\lambda_{Gr\_5} \approx 600$–1400 nm. The long wavelength limits of their spectral ranges, $\lambda_{Gr\_1} \approx 950$ nm and $\lambda_{Gr\_5} \approx 1400$ nm, are shifted by ≈450 nm, compared to 150 nm for the Single Bandgap device ($\lambda_{Gr\_1} \approx 1150$ nm and $\lambda_{Gr\_5} \approx 1300$ nm). For the Single Bandgap device, the redshift from top graphene layer to bottom graphene layer is due to the increase in absorption depth with increasing wavelength. The extra graphene and QD layer of the Multi-Bandgap device (Gr-5 at a depth of 1350 nm for Multi-Bandgap device, compared to Gr-4 at a depth of 1050 nm for Single Bandgap device) would induce an additional redshift, but it cannot account for large difference in redshift between the two types of devices. Therefore, the larger redshift for the Multi-Bandgap device is mostly due to the different bandgaps of QDs used in Multi-Bandgap device. The smaller bandgap QDs at the bottom of the device are more responsive to the longer wavelength photons that penetrate to that depth.[42] As the spectral response for the graphene layers follows the absorption spectrum of the QDs, the shifts in spectral photocurrent response from Gr-1 to Gr-5 (450 nm) clearly reflect the shift in exciton peak and absorption spectrum from QD-1 to QD-3 (500 nm). The normalized photocurrent as function of depth, using the depth location of the Gr layers is shown in Figure 6e. This plot clearly shows that for short wavelengths of $\lambda \approx 400$–600 nm (blue traces), the normalized photocurrent decreases from top to bottom graphene layers. Then, for $\lambda \approx 900$ nm the normalized photocurrent seems to be uniform through the different Gr layers. Then, for $\lambda \approx 1000$–1400 nm (purple traces), the normalized photocurrent clearly increases for deeper layers, which is a direct consequence of the decreasing bandgap profile of the QDs. These wavelengths (low-energy photons) cannot be absorbed by large bandgap QDs on top, but as they reach bottom layers with QDs with lower bandgaps, their absorption increases. Finally, for $\lambda > 1400$ nm (red traces like $\lambda \approx 1800$ nm), even the QD-3 layers cannot absorb photons and the layer becomes practically transparent with zero photoresponse. This behavior can be quantified again by fitting the normalized photocurrent versus depth to an exponential $\approx \exp(-\gamma z)$ to characterize the decay with the normalized photocurrent coefficient "γ" as shown in Figure 6f (see Figure S5b, Supporting Information for fittings). This plot shows that short wavelengths, $\lambda < 800$ nm,

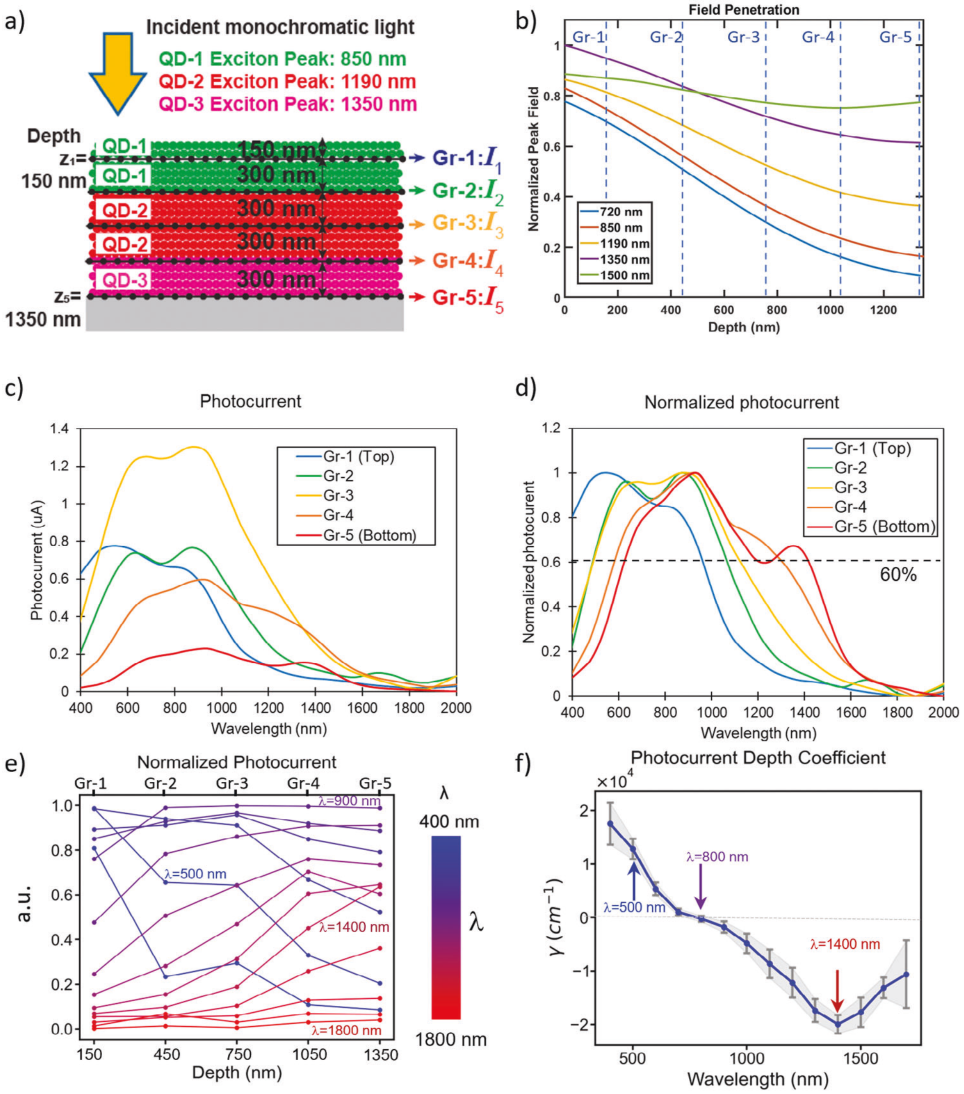

Figure 6. Multi-Bandgap device. a) Device with five graphene layers intercalated with five layers of PbS QDs made of three different sizes. b) FEM simulations of light penetration as a function of wavelength with dashed vertical lines indicating the positions of the graphene collectors. c) Photocurrent from each graphene layer at a bias voltage of 100 mV showing a different response for each graphene layer. d) Photocurrent from c) normalized to their own maximum,illustrating the different spectral band response for each graphene layer. e) Normalized photocurrent from d) at different depths corresponding to the location of the four graphene layers for different wavelengths λ:400−1700 nm in steps of 100 nm, showing decaying responses for short λ:400−600 nm, and growing responses for long λ:900−1400 nm. f) Normalized photocurrent depth coefficient (γ) assuming an exponential decay ≈exp $(-\gamma z)$, showing negative coefficients for $\lambda > 800$ nm.

have normal positive coefficients, while longer wavelengths, $\lambda \approx$ 800–1400 nm, have negative coefficients. Once the wavelength goes beyond the QD absorption edge ($\lambda > 1400$ nm) the film becomes transparent, and the coefficients return to zero. Since we have different QDs, "γ" represents an effective device response for the 5Gr/5QD stack rather than a physical property of any of the QD layers. However, it is interesting to observe negative normalized photocurrent coefficients for $\lambda > 800$ nm that reflect that longer wavelengths are absorbed more efficiently at deeper levels due to our decreasing bandgap profile. These results show that using the Multi-Bandgap configuration with multiple QDs enables not only to extend the spectral range, but also for easier identification of long wavelengths by a finite negative coefficient "γ", instead of the $\gamma \rightarrow 0$ decaying behavior that is more difficult to quantify for the Single-Bandgap case. With QDs of different sizes, the photocurrent depth coefficients of the Multi-Bandgap device can be correlated to each incident wavelength between 400 and 1400 nm, enabling wavelength identification and spectral analysis. The time responses for the Multi-Bandgap devices are shown in Figure 5b. The rise time for the graphene layers from top (Gr-1) to bottom (Gr-5) are 68, 140, 62, 51, and 41 ms. The average for the five graphene layers is 72 ms. The recovery times from top to bottom are 22 0190, 230, 270, and 140 ms, with an average for the five layers of 210 ms. However, the recovery times also show a slower component of ≈2 s associated with surface traps as discussed previously for the Single-Bandgap devices.

The time fittings are shown in the Figure S6b (Supporting Information)

4. Discussion

The devices presented herein show important fabrication achievements toward spectral analysis using only the wavelength dependent penetration depth by means of intercalated graphene collectors with independent electrodes into a bandgap tunable light absorption film made of QDs. Our Single-Bandgap device (Figure 1a) allows to probe the absorption depth of light in a QD film, which potentially can be used to identify the wavelength of monochromatic or narrow band sources. In the case of the Multi-Bandgap devices (Figure 1b), we show an expanded spectral response by incorporating materials with different bandgaps and even achieve negative photocurrent, which is important to identify longer wavelengths. However, our devices still have a significant spectral overlap for different graphene layers, which prevents us from assigning an exclusive spectral range to each graphene layer. Further developments are required to separate the spectral response from each graphene layer. From the fabrication perspective, QDs layers much thicker than the penetration depth may be required to work as filters to reduce the response of graphene layers located at deeper levels. However, thicker layers may also result in more defects using spin coating methods. Incorporating insulating layers to prevent possible electrical cross-talking between different graphene layers can also reduce the overlap in spectral response. However, adding such insulating layers may bring challenges due to the low-temperature restrictions and chemical sensitivity of the QD layers. From the data analysis, more advanced techniques in data science and machine learning can also be used to extract more information from the devices using large data collection and regression analysis. In addition, the different coupling and photocurrent levels in the Multi-Bandgap devices highlight the need for better understanding and improvements in surface chemistry to enhance or control the transfer of photocarriers from QDs to Gr. Advances in graphene transfer and QD solution processing and coating are also required to enhance the reliability and fabrication throughput.

Compared to previous literature reports, our results offer significant advantages but also present significant challenges. Pejovic et al reported a vertically-stacked dual-band (NIR and SWIR) photodetector that can cover the $\lambda \approx 400-1400$ nm range.[56] In a similar configuration, Tang et al reported also a vertically-stacked dual-band QD photodetector but extending the spectral response into the MWIR $\lambda \approx 3000$ nm using HgTe QDs.[29] Our intercalated devices offered a multi channel band response, showing up to five graphene channels, however, our PbS QDs cannot reach the MWIR range. Integrating different materials with different bandgaps could allow us to reach both deeper UV ranges and longer IR (MWIR) ranges, but that is still a challenge to be demonstrated in our configuration. In a lateral patterning configuration, Tang et al demonstrated three channel QD based multispectral photodetector using planar configuration with three-pixels array covering the MWIR range.[33] However, a filter is still required to enhance the optical resolution. In our case, our vertical stacking avoids to couple lateral resolution with spectral range. Compared with conventional multispectral detectors, our Gr/QD photodetectors offer large spectral range, but its low mobility and defects still prevent higher speeds compared to crystalline films like Si and Ge.

5. Conclusion

In conclusion, we have presented a novel technology of intercalated QDs and Gr monolayers, demonstrating for the first time independent electrodes for each graphene monolayer, allowing to probe the light absorption as a function of depth by means of the photocurrent of the graphene layers. As a proof of principle, our devices with a single type of QDs (Single-Bandgap) clearly show that short wavelengths are mainly absorbed at the top with rapid photocurrent decays through the stack, while deeper graphene layers respond only to the longer wavelengths that have deeper penetration depths to reach the bottom of the stack. This device behavior is quantified by a parameter we call the photocurrent depth coefficient "γ" that is obtained by fitting the normalized photocurrent to a decaying exponential function $exp\ (-\gamma z)$, showing large coefficients for short wavelengths and $\gamma \rightarrow 0$ for long wavelengths. A major improvement is the integration of QDs with different sizes, decreasing the bandgap of the QDs from top to bottom. This enables not only to extend the spectral response, but also to achieve finite negative photocurrent depth coefficients for long wavelengths which can facilitate the identification of infrared components. These "γ" coefficients encode the device response and offer a new alternative for wavelength discrimination and identification for spectral analysis. This technology does not require any long-path dispersive or interferometer components, resulting in a very compact (≈1 µm) thin film with potential spectral analysis capabilities. However, further work is required to fully exploit this technology. A better understanding of the charge transfer between QDs of different types and graphene is required to account for the differences in response of the QD-Gr system. The presented fabrication process also requires further optimization to be integrated with semiconductor foundries for large scale manufacturing. Further experiments are required such as time-resolved PL, UV photoelectron spectroscopy, and transient photovoltage to identify band-alignment and charge transfer mechanisms between Graphene and Quantum Dots and experimentally verify the role that charge transfer plays in the performance of these devices in addition to optical absorption. Future work addressing stability is also important, especially concerning the effect on long-time stability of humidity conditions, passivation layers, and graphene intercalation. Furthermore, improving the design and fabrication technology are required to decrease the spectral overlapping, as well as developing new data analysis methods and algorithms to enable spectral analysis from the collective response of the Gr charge collecting layers.

6. Experimental Section

PbS Quantum Dot Synthesis: 940 mg of lead oxide (PbO) was dissolved in 25 ml of 1-octadecene (ODE) with different amounts of oleic acid from 3.5 to 35 ml to achieve various extinction peak of absorption spectrum from 850 to 1350 nm. And then, the solution was degassed under vacuum at 90 °C for two hours to be perfectly dissolved. The sulfur precursor (420 μl of bis(trimethylsilyl) sulfide in 12.8 ml of ODE) was injected in the solution when the color of solution became clear. After that, the solution was allowed to react for 30 s and then cooled it down by placing the flask in water. The color of the solution becomes dark brown. Next, the PbS QDs was separated from the raw solution by centrifugation, followed by cleaning with toluene and acetone with three times to obtain high purity QDs. After the cleaning process, PbS QDs was dissolved in toluene to disperse, and then filtered with a 0.25 um pore size filter.

Quantum Dot Deposition: PbS QDs film was deposited using spin-coating under ambient atmosphere. For each PbS QDs layer, the QDs solution (30 mg ml^{-1} in toluene) was spin-casted at 2500 rpm for 30 s, then a solid-state ligand exchange was performed by flooding the surface with 0.03 M TBAI in methanol for 30 s before spinning dry at 2500 rpm. For the bottom Gr/QD system, QDs film was formed layer-by-layer.

Spectral Characterization: The spectral response of intercalated graphene and quantum dots multispectral photodetectors was measured using a source meter (Keithley 2400) under a Xe lamp and filters (66 485-500HX-R1, USFW-100, Newport) equipped with a monochromator (CS260-RG-3-FH-D, Newport). The beam size of light (approximately 2 mm × 4 mm) was enough to cover the channel of the sample. Then, the spectral response of multispectral photodetectors was measured with 10 nm step for 5 s to obtain the accurate response from illuminated wavelength.

Supporting Information

Supporting Information is available from the Wiley Online Library or from the author.

Acknowledgements

S.A. and J.Y.S. contributed equally to this work. This work was supported by the National Science Foundation under Award No. 2046176 (NSF CAREER) and by the Air Force Office of Scientific Research (FA9550-22-1-0312). This work was performed, in part, at the San Diego Nanotechnology Infrastructure (SDNI) of UCSD, NANO3, a member of the National Nanotechnology Coordinated Infrastructure, which was supported by the National Science Foundation (Grant No. ECCS-1542148). Seungbae Ahn was supported by the Kwanjeong Fellowship from the Kwanjeong Educational Foundation.

Conflict of Interest

The authors declare no conflict of interest.

Data Availability Statement

The data that support the findings of this study are available from the corresponding author upon reasonable request.

Keywords

2D materials, absorption coefficient, graphene, multispectral, penetration depth, photodetectors, quantum dots

Received: June 2, 2024

---

[1] N. S. Savage, *Nat. Photonics* **2009**, *3*, 601.
[2] A. Li, C. Yao, J. Xia, H. Wang, Q. Cheng, R. Penty, Y. Fainman, S. Pan, *Light: Sci. Appl.* **2022**, *11*, 174.
[3] C. P. Bacon, Y. Mattley, R. DeFrece, *Rev. Sci. Instrum.* *75*, 16.
[4] C. D. Tran, *Fresenius. J. Anal. Chem.* **2001**, *369*, 313.
[5] Q. Li, X. He, Y. Wang, H. Liu, D. Xu, F. Guo, *J. Biomed. Opt.* **2013**, *18*, 100901.
[6] J. H. Rouse, J. A. Shaw, R. L. Lawrence, J. L. Lewicki, L. M. Dobeck, K. S. Repasky, L. H. Spangler, *Environ. Earth Sci.* **2010**, *60*, 313.
[7] S. Kim, D. Cho, J. Kim, M. Kim, S. Youn, J. E. Jang, M. Je, D. H. Lee, B. Lee, D. L. Farkas, J. Y. Hwang, *Biomed. Opt. Express* **2016**, *7*, 5294.
[8] G. Jung, S. Kim, J. G. Kim, In *Photonics in Dermatology and Plastic Surgery*, (Eds: B. Choi, H. Zeng, N. Kollias), SPIE, Bellingham, WA **2017**, p. 26.
[9] L. Rey-Barroso, F. J. Burgos-Fernández, X. Delpueyo, M. Ares, S. Royo, J. Malvehy, S. Puig, M. Vilaseca, *Sensors* **2018**, *18*, 1441.
[10] Z. Wang, B. Li, L. Li, *IOP Conf. Ser. Earth Environ. Sci.* **2019**, *237*, 032087.
[11] J. Hodgkinson, R. P. Tatam, *Meas. Sci. Technol.* **2013**, *24*, 012004.
[12] S. Baek, E. Choi, Y. Baek, C. Lee, *Digit. Signal Process. A Rev. J.* **2018**, *78*, 294.
[13] A. Sahar, S. Zainab, M. I. Khan, A. Saleem, U. Rahman, M. M. Arif Chaudhry, In *Advances in Noninvasive Food Analysis*, CRC Press, Boca Raton, FL **2019**, pp. 9.
[14] A. M. C. Davies, A. Grant, *Int. J. Food Sci. Technol.* **1987**, *22*, 191.
[15] J. Vargas, S. Alsweiss, O. Toker, R. Razdan, J. Santos, *Sensors* **2021**, *21*, 5397.
[16] Z. Ballard, C. Brown, A. M. Madni, A. Ozcan, *Nat. Mach. Intell.* **2021**, *3*, 556.
[17] N. Hagen, M. W. Kudenov, *Opt. Eng.* **2013**, *52*, 090901.
[18] P. J. Lapray, X. Wang, J. B. Thomas, P. Gouton, *Sensors* **2014**, *14*, 21626.
[19] C. Wang, J. Zhao, H. Cao, C. Shen, J. Tang, J. Liu, *Opt. Express* **2023**, *31*, 33776.
[20] L. Wang, B.-H. Chen, C.-Y. Fang, J. He, C.-Y. Wu, X. Zhang, X.-P. Yang, J.-B. Mao, J.-G. Hu, L.-B. Luo, *IEEE Trans. Electron Devices* **2022**, *69*, 3258.
[21] J. B. Bates, *Science* **1976**, *191*, 31.
[22] H. H. Richardson, V. W. Pabst, J. A. Butcher, *Appl. Spectrosc.* **1990**, *44*, 822.
[23] S. M. Alawi, T. Krug, H. H. Richardson, *Appl. Spectrosc.* **1993**, *47*, 1626.
[24] J. Yuan, Y. Chen, A. L. Holmes, J. C. Campbell, *IEEE J. Quantum Electron.* **2014**, *50*, 1.
[25] M. C. M. M. Souza, A. Grieco, N. C. Frateschi, Y. Fainman, *Nat. Commun.* **2018**, *9*, 665.
[26] J. Liu, D. Hu, M. Ni, Y. Zou, Y. Gu, Z. Han, J. Li, Y. He, Z. Zhang, X. Xu, *J. Phys. Chem. Lett.* **2022**, *13*, 3659.
[27] S. Yuan, D. Naveh, K. Watanabe, T. Taniguchi, F. Xia, *Nat. Photonics* **2021**, *15*, 601.
[28] S. V. Solanke, S. Rathkanthiwar, A. Kalra, R. K. Mech, M. Rangarajan, S. Raghavan, D. N. Nath, *Semicond. Sci. Technol.* **2019**, *34*, 075020.
[29] X. Tang, M. M. Ackerman, M. Chen, P. Guyot Sionnest, *Nat. Photonics* **2019**, *13*, 277.
[30] X. Tang, M. M. Ackerman, P. Guyot-Sionnest, *Laser Photon. Rev.* **2019**, *13*, 1900165.
[31] D. J. Norris, *Nat. Photonics* **2019**, *13*, 230.
[32] S. Zhang, C. Bi, Y. Tan, Y. Luo, Y. Liu, J. Cao, M. Chen, Q. Hao, X. Tang, *ACS Nano* **2022**, *16*, 18822.
[33] X. Tang, X. Tang, K. W. C. Lai, *ACS Photonics* **2016**, *3*, 2396.
[34] S. Ahn, W. Chen, M. A. Moreno-Gonzalez, M. Lockett, J. Wang, O. Vazquez-Mena, *Adv. Electron. Mater.* **2020**, *6*, 2000014.
[35] W. Chen, S. Ahn, M. Balingit, J. Wang, M. Lockett, O. Vazquez-Mena, *Nanoscale* **2020**, *12*, 4909.
[36] W. Chen, S. Ahn, C. Rangel, O. Vazquez-Mena, *Front. Mater.* **2019**, *6*, 159.

[37] W. Chen, J. Castro, S. Ahn, X. Li, O. Vazquez-Mena, *Adv. Mater.* **2019**, *31*, 1807894.
[38] G. Konstantatos, M. Badioli, L. Gaudreau, J. Osmond, M. Bernechea, F. P. G. de Arquer, F. Gatti, F. H. L. Koppens, *Nat. Nanotechnol.* **2012**, *7*, 363.
[39] D. Zhang, L. Gan, Y. Cao, Q. Wang, L. Qi, X. Guo, *Adv. Mater.* **2012**, *24*, 2715.
[40] Z. Sun, Z. Liu, J. Li, G. A. Tai, S. P. Lau, F. Yan, *Adv. Mater.* **2012**, *24*, 5878.
[41] G. B. Barin, Y. Song, I. D. F. Gimenez, A. G. S. Filho, L. S. Barreto, J. Kong, *Carbon N. Y.* **2015**, *84*, 82.
[42] S. Ahn, H. Chung, W. Chen, M. A. Moreno-Gonzalez, O. Vazquez-Mena, *J. Chem. Phys.* **2019**, *151*, 234705.
[43] C. M. Chuang, P. R. Brown, V. Bulović, M. G. Bawendi, *Nat. Mater.* **2014**, *13*, 796.
[44] P. R. Brown, D. Kim, R. R. Lunt, N. Zhao, M. G. Bawendi, J. C. Grossman, V. Bulović, *ACS Nano* **2014**, *8*, 5863.
[45] D. D. Wanger, R. E. Correa, E. A. Dauler, M. G. Bawendi, *Nano Lett.* **2013**, *13*, 5907.
[46] X. Lan, O. Voznyy, F. P. García de Arquer, M. Liu, J. Xu, A. H. Proppe, G. Walters, F. Fan, H. Tan, M. Liu, Z. Yang, S. Hoogland, E. H. Sargent, *Nano Lett.* **2016**, *16*, 4630.
[47] A. Stavrinadis, S. Pradhan, P. Papagiorgis, G. Itskos, G. Konstantatos, *ACS Energy Lett.* **2017**, *2*, 739.
[48] X. Lan, O. Voznyy, A. Kiani, F. P. García de Arquer, A. S. Abbas, G.-H. Kim, M. Liu, Z. Yang, G. Walters, J. Xu, M. Yuan, Z. Ning, F. Fan, P. Kanjanaboos, I. Kramer, D. Zhitomirsky, P. Lee, A. Perelgut, S. Hoogland, E. H. Sargent, *Adv. Mater.* **2016**, *28*, 299.
[49] S. Ahn, O. Vazquez-Mena, *J. Chem. Phys.* **2022**, *156*, 739.
[50] B. Jalali, M. Paniccia, G. Reed, *IEEE Microw. Mag.* **2006**, *7*, 58.
[51] U. Bothra, M. Albaladejo-Siguan, Y. Vaynzof, D. Kabra, *Adv. Opt. Mater.* **2023**, *11*, 2201897.
[52] M. Zhang, W. Liu, Y. Gong, Q. Liu, Z. Chen, *Adv. Opt. Mater.* **2022**, *10*, 2201889.
[53] M. Vafaie, J. Z. Fan, A. Morteza Najarian, O. Ouellette, L. K. Sagar, K. Bertens, B. Sun, F. P. García de Arquer, E. H. Sargent, *Matter* **2021**, *4*, 1042.
[54] X. Tang, M. Chen, A. Kamath, M. M. Ackerman, P. Guyot-Sionnest, *ACS Photonics* **2020**, *7*, 1117.
[55] I. Nikitskiy, S. Goossens, D. Kufer, T. Lasanta, G. Navickaite, F. H. L. Koppens, G. Konstantatos, *Nat. Commun.* **2016**, *7*, 11954.
[56] V. Pejović, E. Georgitzikis, I. Lieberman, P. E. Malinowski, P. Heremans, D. Cheyns, *Adv. Funct. Mater.* **2022**, *32*, 2201424.